J. Fluid Mech. (2002), *vol.* 461, *pp.* 365–386. © 2002 Cambridge University Press
DOI: 10.1017/S0022112002008509 Printed in the United Kingdom

Laminar flow past a sphere rotating in the streamwise direction

By DONGJOO KIM AND HAECHEON CHOI†
School of Mechanical and Aerospace Engineering, Seoul National University, Seoul 151-742, Korea

(Received 7 June 2001 and in revised form 10 January 2002)

Numerical simulations are conducted for laminar flow past a sphere rotating in the streamwise direction, in order to investigate the effect of the rotation on the characteristics of flow over the sphere. The Reynolds numbers considered are $Re = 100$, 250 and 300 based on the free-stream velocity and sphere diameter, and the rotational speeds are in the range of $0 \leqslant \omega^* \leqslant 1$, where ω^* is the maximum azimuthal velocity on the sphere surface normalized by the free-stream velocity. At $\omega^* = 0$ (without rotation), the flow past the sphere is steady axisymmetric, steady planar-symmetric, and unsteady planar-symmetric, respectively, at $Re = 100$, 250 and 300. Thus, the time-averaged lift forces exerted on the stationary sphere are not zero at $Re = 250$ and 300. When the rotational speed increases, the time-averaged drag force increases for the Reynolds numbers investigated, whereas the time-averaged lift force is zero for all $\omega^* > 0$. On the other hand, the lift force fluctuations show a non-monotonic behaviour with respect to the rotational speed. At $Re = 100$, the flow past the sphere is steady axisymmetric for all the rotational speeds considered and thus the lift force fluctuation is zero. At $Re = 250$ and 300, however, the flows are unsteady with rotation and the lift force fluctuations first decrease and then increase with increasing rotational speed, showing a local minimum at a specific rotational speed. The vortical structures behind the sphere are also significantly modified by the rotation. For example, at $Re = 300$, the flows become 'frozen' at $\omega^* = 0.5$ and 0.6, i.e. the vortical structures in the wake simply rotate without temporal variation of their strength and the magnitude of the instantaneous lift force is constant in time. It is shown that the flow becomes frozen at higher rotational speed with increasing Reynolds number. The rotation speed of the vortical structures is shown to be slower than that of the sphere.

1. Introduction

Flow over a sphere is of interest in many engineering applications associated with particle transport, because a solid particle is generally modelled as a sphere. Solid particles in a flow translate and rotate simultaneously, where the rotation in the streamwise or transverse direction may be induced by particle–particle or particle–wall collisions. Therefore, flow over a rotating sphere has received much attention and it is important to understand the effect of rotation on the flow.

The characteristics of flow over a sphere depend significantly on the direction of rotation. One important direction of rotation is the transverse direction, where the

† Author to whom correspondence should be addressed: choi@socrates.snu.ac.kr. Also at National CRI Center for Turbulence and Flow Control Research, Institute of Advanced Machinery and Design, Seoul National University.

https://doi.org/10.1017/S0022112002008509 Published online by Cambridge University Press

rotational direction is orthogonal to that of translation. The other is the streamwise direction, where the rotational direction is the same as that of translation. In case of the transverse rotation, quite a few studies have been conducted focusing on the relation between the rotational speed and the force (drag and lift) exerted on the sphere (Rubinow & Keller 1961; Barkla & Auchterlonie 1971; Tsuji, Morikawa & Mizuno 1985; Oesterlé & Dinh 1998; Kurose & Komori 1999). However, only a few studies have been conducted for the case of streamwise rotation and thus only a little knowledge has been obtained. One may refer to Schlichting (1979) where previous results on flow over a streamwisely rotating sphere have been summarized. Two specific features of such a flow were introduced by Schlichting. First, the drag and the critical Reynolds number, at which the drag coefficient decreases abruptly, depend strongly on the rotational speed (Luthander & Rydberg 1935). Second, the line of separation is moved upstream due to the rotation (Hoskin 1955). The physical reason for this effect is that the centrifugal force, acting on the fluid particles rotating with the sphere in the boundary layer, has the same effect as an additional adverse pressure gradient. However, to the best of our knowledge, there has been no investigation of the effect of the streamwise rotation on the lift force exerted on the sphere and the flow characteristics behind the sphere.

The objective of this work is to numerically investigate the effect of the streamwise rotation on the characteristics of flow over a sphere such as the drag, lift and vortical structures. In particular, the modification of three-dimensional vortical structures due to the rotation is focused on in this study. The present numerical method is based on an immersed boundary method in a cylindrical coordinate system (Kim, Kim & Choi 2001). The computations are performed for laminar flow at $Re = 100$, 250 and 300 in the range of $0 \leqslant \omega^* \leqslant 1$, where ω^* is the non-dimensional angular velocity of the rotating sphere (the maximum azimuthal velocity on the sphere surface normalized by the free-stream velocity u_∞). Flow over a stationary sphere is first simulated and compared with the previous numerical and experimental results and then flow over a rotating sphere is computed in order to understand the effect of the rotation.

2. Numerical details

Flow behind a sphere shows completely unsteady three-dimensional phenomena even at low Reynolds numbers (Sakamoto & Haniu 1990; Johnson & Patel 1999; Mittal 1999*a*,*b*). Even though the geometry is very simple, flows over a sphere with and without rotation have been studied mostly by experimental methods; only a few numerical results have been published in the literature because it is not easy to numerically simulate the three-dimensional nature of this flow.

So far, there have been two different approaches to the simulation of flow over a sphere. One uses a body-fitted grid, and the other uses an immersed boundary method in cylindrical coordinates. In the case of a body-fitted grid, an O-O type grid in a spherical coordinate system is commonly used, which is generated by rotating a two-dimensional O-type grid in the azimuthal direction (Shirayama 1992; Johnson & Patel 1999; Mittal 1999*a*). In a different body-fitted grid approach, Tomboulides & Orszag (2000) used an unstructured-based grid together with a mixed spectral element/Fourier spectral method.

On the other hand, the immersed boundary method was originally developed for simulation of flow over a complex geometry, where the body in the flow is treated as momentum forcing in the Navier–Stokes equations rather than a real body. Therefore, with this method, flow over a sphere can be easily handled with orthogonal

https://doi.org/10.1017/S0022112002008509 Published online by Cambridge University Press

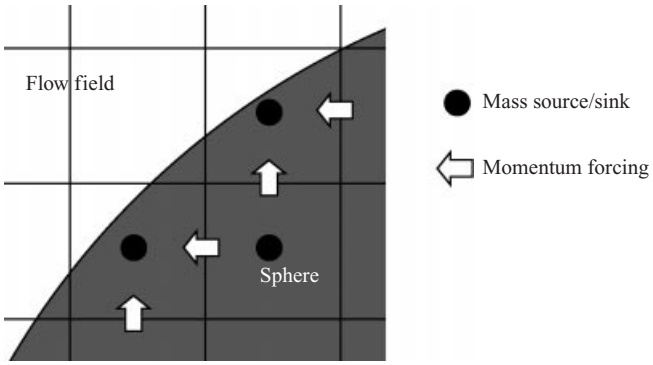


FIGURE 1. Schematic diagram of the present immersed boundary method. The shaded area denotes the sphere and the lines denote grid lines.

(cylindrical) grids that do not coincide with the sphere surface. Recently, it has been demonstrated that the immersed boundary method can accurately simulate laminar flow over a stationary sphere (Fadlun *et al.* 2000; Kim *et al.* 2001).

In the present study, we use an immersed boundary method in cylindrical coordinates proposed by Kim *et al.* (2001). In their approach, a mass source/sink is also introduced near an immersed boundary in order to enhance the quality of the solution by satisfying the continuity for the cell containing the immersed boundary. Figure 1 is a schematic diagram of the present immersed boundary method using the concept of momentum forcing and mass source/sink.

The governing equations for unsteady incompressible viscous flow are

$$\frac{\partial u_i}{\partial t} + \frac{\partial u_i u_j}{\partial x_j} = -\frac{\partial p}{\partial x_i} + \frac{1}{Re}\frac{\partial^2 u_i}{\partial x_j \partial x_j} + f_i, \tag{2.1}$$

$$\frac{\partial u_i}{\partial x_i} - q = 0, \tag{2.2}$$

where x_i are the cylindrical coordinates, u_i are the corresponding velocity components, p is the pressure, f_i and q, respectively, are the momentum forcing and the mass source/sink defined on the immersed boundary or inside the body. A staggered grid system is employed in this study, and thus u_i and f_i are defined at the cell face, whereas p and q are defined at the cell centre. All the variables are non-dimensionalized by the sphere diameter d, and the free-stream velocity u_∞. Re denotes the Reynolds number, defined as $Re = u_\infty d/\nu$. Here, ν is the kinematic viscosity.

The time-integration method used to solve (2.1) and (2.2) is based on a fractional-step method where a pseudo-pressure is used to correct the velocity field such that the continuity equation is satisfied at each computational time step. In this study, we use a second-order semi-implicit time advancement scheme as in Akselvoll & Moin (1996), who proposed a kind of domain decomposition approach in order to increase the computational efficiency in a cylindrical coordinate system. That is, in the core region ($0 \leqslant r < r_c$), convection and diffusion terms with derivatives in the azimuthal direction are treated implicitly and the remaining terms explicitly, whereas in the outer region ($r > r_c$), convection and diffusion terms with derivatives in the radial direction are treated implicitly and the remaining terms explicitly. This procedure simplifies the solution algorithm because only one component of the discretized momentum

https://doi.org/10.1017/S0022112002008509 Published online by Cambridge University Press

equation is nonlinear in each region. The interface ($r = r_c$) between the core and outer regions is determined such that the time step restriction associated with numerical instability is minimized. In this study, the interface is located at $r \approx 0.1d$. In both regions, a third-order Runge–Kutta method (RK3) is used for the terms treated explicitly and a second-order Crank–Nicolson method is used for the terms treated implicitly:

$$\frac{\hat{u}_i^k - u_i^{k-1}}{\Delta t} = -2\alpha_k \frac{\partial p^{k-1}}{\partial x_i} + \alpha_k B(\hat{u}_i^k) + \alpha_k B(u_i^{k-1}) + \gamma_k A(u_i^{k-1}) + \rho_k A(u_i^{k-2}) + f_i^k, \quad (2.3)$$

$$\frac{\partial^2 \phi^k}{\partial x_i \partial x_i} = \frac{1}{2\alpha_k \Delta t}\left(\frac{\partial \hat{u}_i^k}{\partial x_i} - q^k\right), \quad (2.4)$$

$$u_i^k = \hat{u}_i^k - 2\alpha_k \Delta t \frac{\partial \phi^k}{\partial x_i}, \quad (2.5)$$

$$p^k = p^{k-1} + \phi^k, \quad (2.6)$$

where A and B are the operators on the velocity vector, $\hat{u}_i$ is the intermediate velocity and ϕ is the pseudo-pressure. A includes terms treated explicitly and B includes terms treated implicitly, as mentioned before. Also, Δt and k are the computational time step and substep index, respectively, and $\alpha_k, \gamma_k, \rho_k$ are the coefficients of RK3 ($\alpha_1 = 4/15$, $\gamma_1 = 8/15$, $\rho_1 = 0$; $\alpha_2 = 1/15$, $\gamma_2 = 5/12$, $\rho_2 = -17/60$; $\alpha_3 = 1/6$, $\gamma_3 = 3/4$, $\rho_3 = -5/12$).

Note that in order to obtain $\hat{u}_i^k$ from (2.3), the momentum forcing f_i^k has to be determined in advance such that u_i^k satisfies the boundary condition on the immersed boundary (e.g. a no-slip condition on the stationary sphere surface). Similarly, the mass source q^k also has to be determined in advance in order to obtain ϕ^k from (2.4). In this study, we use the method proposed by Kim *et al.* (2001) for evaluation of f_i^k and q^k.

Figure 2 shows the coordinate system, boundary conditions and a typical mesh near the sphere. As explained before, we use a cylindrical coordinate system, where x, r and θ, respectively, denote the streamwise, radial and azimuthal directions. A Cartesian coordinate system (x, y, z) is also defined in order to present the drag and lift forces, where the lift force is composed of two orthogonal (y and z) components. The computational domain used is $-15d \leqslant x \leqslant 15d$, $0 \leqslant r \leqslant 15d$, and $0 \leqslant \theta \leqslant 2\pi$, where ($x = 0$, $r = 0$) corresponds to the centre location of the sphere. A Dirichlet boundary condition ($u_x = u_\infty$, $u_r = 0$, $u_\theta = 0$) is used at the inflow and far-field boundaries, and a convective boundary condition ($\partial u_i/\partial t + c\partial u_i/\partial x = 0$) is used for the outflow boundary, where c is the space-averaged streamwise velocity at the exit. Non-uniform meshes are used with dense resolution at $r \simeq 0.5d$ for accurately capturing the separating shear layer around the sphere. The numbers of grid points are $145(x) \times 61(r) \times 40(\theta)$, $193(x) \times 91(r) \times 40(\theta)$ and $289(x) \times 161(r) \times 40(\theta)$, respectively, for $Re = 100$, 250 and 300. The current mesh and domain size have been determined from an extensive study of the numerical parameters (e.g. computational domain size, number of grid points, resolution near the sphere surface, etc.). In the case of the rotating sphere, the direction of the rotation is streamwise (x-direction) as shown in figure 2 and the non-dimensional rotational speed ($\omega^* = \omega R/u_\infty$) investigated is $0 \leqslant \omega^* \leqslant 1$, where ω is the angular velocity of the streamwise rotation and R is the radius of the sphere.

https://doi.org/10.1017/S0022112002008509 Published online by Cambridge University Press

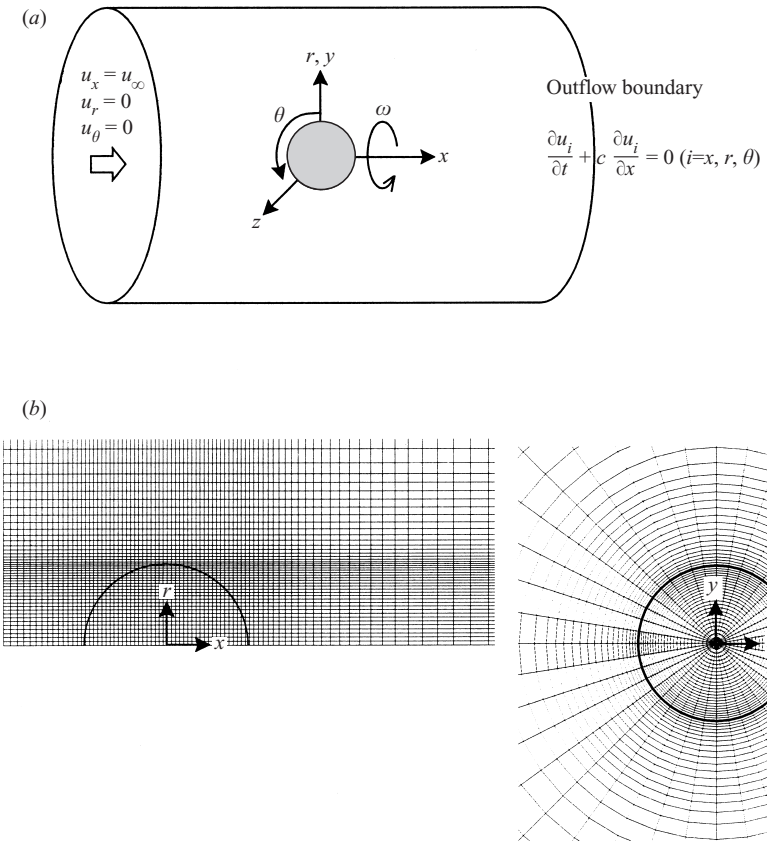


FIGURE 2. (*a*) Coordinate system and boundary conditions; (*b*) typical mesh near the sphere ($Re = 100$).

3. Flow past a stationary sphere

For the validation of the present numerical method and comparison with the characteristics of flow past a rotating sphere, laminar flow past a stationary sphere is first simulated at three different Reynolds numbers ($Re = 100$, 250 and 300). Flows at these Reynolds numbers represent three different laminar-flow regimes: steady axisymmetric flow ($Re \leqslant 200$), steady planar-symmetric flow ($210 \leqslant Re \leqslant 270$) and unsteady planar-symmetric flow ($280 \leqslant Re < 375$) (Johnson & Patel 1999; Mittal 1999*a*,*b*; Tomboulides & Orszag 2000).

Figure 3 shows the three-dimensional vortical structures behind a stationary sphere at three Reynolds numbers, where the surfaces of vortical structures are identified using the method of Jeong & Hussain (1995). At $Re = 100$, the flow maintains axisymmetry and no vortical structure exists in the wake (figure 3*a*). However, at $Re = 250$, the flow becomes planar-symmetric, losing axisymmetry, and a pair of vortical structures appears in the wake (figure 3*b*). At $Re = 300$, the flow becomes unsteady and the vortices are shed while the planar-symmetry of the flow is maintained. Figure 3(*c*) shows the time sequence of three-dimensional vortical structures during one period (T) at $Re = 300$. At $t = \frac{1}{4}T$, the origin of a vortex (A) is shown to be attached to a vortical region enveloping the sphere. In the following figure ($t = \frac{2}{4}T$), the vortex is shed to convect downstream and the legs develop in the near wake. A

https://doi.org/10.1017/S0022112002008509 Published online by Cambridge University Press

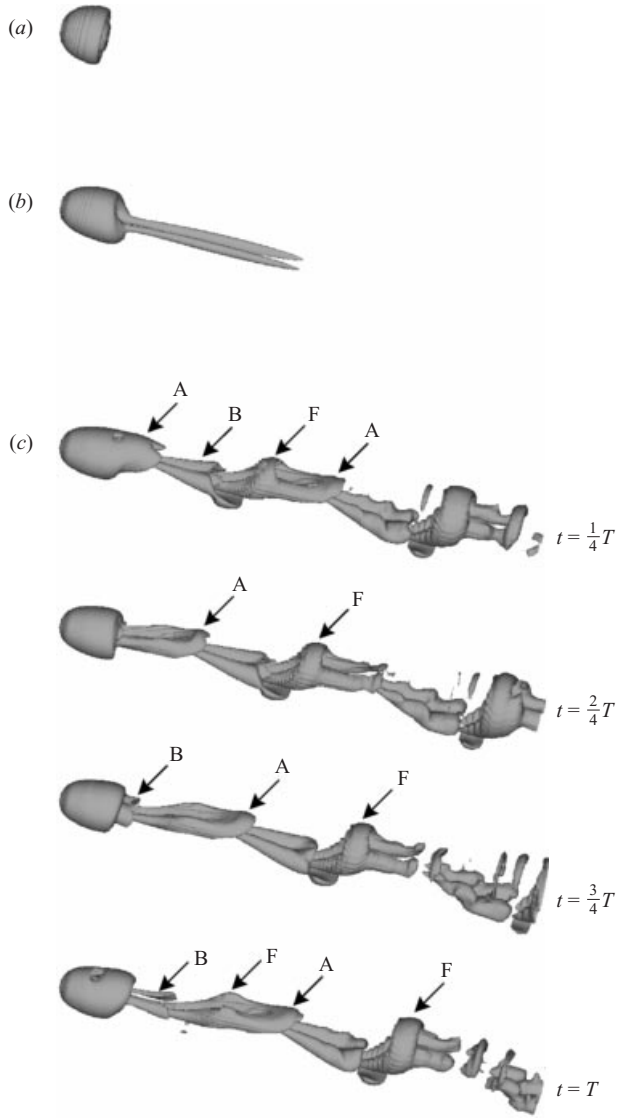


FIGURE 3. Vortical structure behind a stationary sphere: (*a*) $Re = 100$; (*b*) $Re = 250$; (*c*) $Re = 300$. At $Re = 300$, the time sequence of vortical structures is drawn during one period T.

new vortical structure (B) is visible around the legs of vortex A at $t = \frac{3}{4}T$ and is believed to be induced by vortex A (Johnson & Patel 1999). Then this vortex develops downstream to form the legs of a new vortex at $t = T$, and is seen further downstream at a later time ($t = \frac{1}{4}T$). Note that the vortical structures A and B have opposite directions of rotation and different strength, i.e. vortex A is much stronger than B. This process completes one cycle of vortex shedding behind the sphere, which is very similar to the result of Johnson & Patel (1999). It is interesting to note that a new hairpin vortex (F) evolves in the middle of vortex A (at $t = T$) and becomes strongest further downstream. This hairpin-evolution process is very similar to those seen in a transitional boundary layer (Choi 1998) and in an 'artificial' turbulent channel flow (Zhou *et al.* 1999), but hairpin vortex F was not observed by Johnson & Patel (1999).

https://doi.org/10.1017/S0022112002008509 Published online by Cambridge University Press

	Re	$\bar{C}_d$	$\bar{C}_l$	St
Present	100	1.087		
	250	0.702	0.060	
	300	0.657	0.067	0.134
Fornberg (1988)	100	1.085		
Johnson & Patel (1999)	250	0.70	0.062	
	300	0.656	0.069	0.137
Constantinescu & Squires (2000)	250	0.70	0.062	
	300	0.655	0.065	0.136

TABLE 1. Simulation results for flow over a stationary sphere. Here, $\bar{C}_d$ and $\bar{C}_l$ are the time-averaged drag and lift coefficients, respectively.

Table 1 summarizes the results of the present simulation together with the previous numerical results of Fornberg (1988), Johnson & Patel (1999), and Constantinescu & Squires (2000) in which body-fitted grids were used. The drag coefficient at $Re = 100$ agrees very well with that of Fornberg (1988). The drag and lift coefficients at $Re = 250$ and 300 are also in excellent agreement with those of Johnson & Patel (1999) and Constantinescu & Squires (2000). The present Strouhal number ($St = fd/u_\infty$) at $Re = 300$, where f is the vortex shedding frequency, is in good agreement with those of Johnson & Patel (1999) and Constantinescu & Squires (2000). However, all the numerical results for St presented in table 1 are smaller than the experimental result ($St = 0.15$–0.16) of Sakamoto & Haniu (1990).

4. Flow past a rotating sphere

Flows past a rotating sphere are simulated at $Re = 100$, 250 and 300, where flows without rotation are used as initial flow fields. The direction of the rotation is streamwise and the non-dimensional rotational speed ($\omega^* = \omega R/u_\infty$) considered is $0 \leqslant \omega^* \leqslant 1$. The present study focuses on the modification of vortical structures behind the sphere and the variations of drag and lift forces due to the streamwise rotation. As explained below, simulation results show that the flow characteristics are very different depending on both the Reynolds number and the rotational speed.

4.1. *Flow characteristics*

Figure 4 shows the modification of vortical structures due to the rotation at $Re = 100$, where the structures are identified by using the same method as in figure 3. The vortical structures are axisymmetric for all the rotational speeds investigated and have a considerable amount of streamwise-vorticity component (ω_x). Also, with increasing rotational speed, the vortex becomes stronger and elongated in the streamwise direction.

Figure 5 shows the modification of vortical structures due to the rotation at $Re = 250$. Without rotation, a pair of vortices with the same vortical strength but opposite direction of rotation appears in the wake. At $\omega^* = 0.1$, the vortical structure with positive ω_x becomes stronger, but that of negative ω_x is weakened, because the rotation of the sphere induces positive streamwise vorticity in the wake. This effect becomes stronger at $\omega^* = 0.3$, at which the structure with negative ω_x disappears in the wake. However, at $\omega^* \geqslant 0.5$, a structure with negative ω_x is newly induced near that with positive ω_x. At $\omega^* = 1$, the vortical structures with positive and negative ω_x are twisted together in a complex pattern.

https://doi.org/10.1017/S0022112002008509 Published online by Cambridge University Press

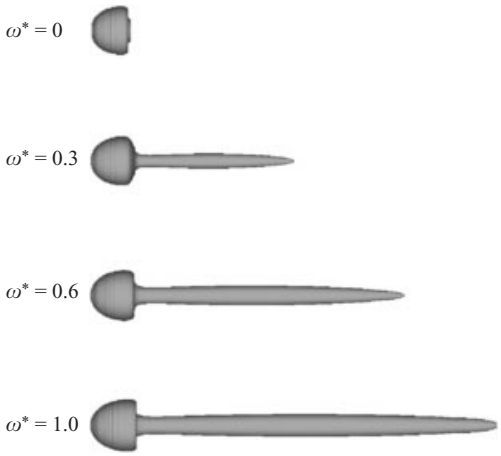


FIGURE 4. Modification of vortical structures due to the rotation at $Re = 100$.

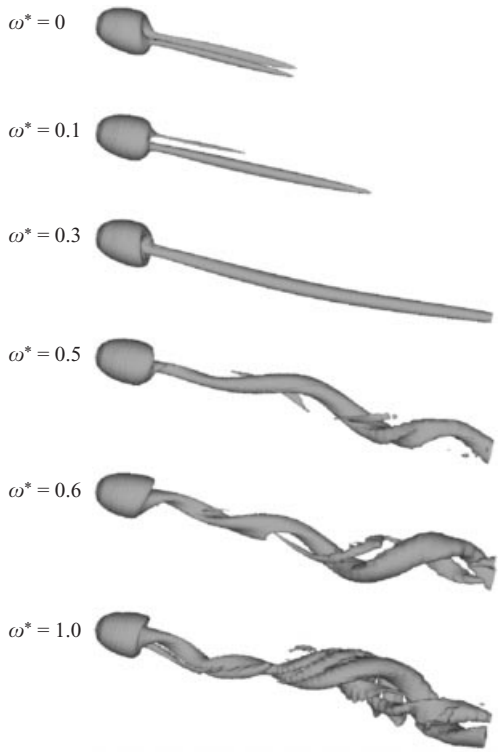


FIGURE 5. Modification of vortical structures due to the rotation at $Re = 250$.

In contrast to the flow at $Re = 100$, the flow at $Re = 250$ becomes unsteady for all the rotational speeds investigated. However, this unsteady flow can be categorized into two different groups according to the temporal evolution of vortical structures: at small rotational speeds ($\omega^* = 0.1$ and 0.3), the vortical structures are 'frozen' in a rotating coordinate, whereas they are unsteady asymmetric at large rotational speeds ($\omega^* \geqslant 0.5$). The difference between frozen and unsteady asymmetric flows is illustrated in figures 6 and 7.

https://doi.org/10.1017/S0022112002008509 Published online by Cambridge University Press

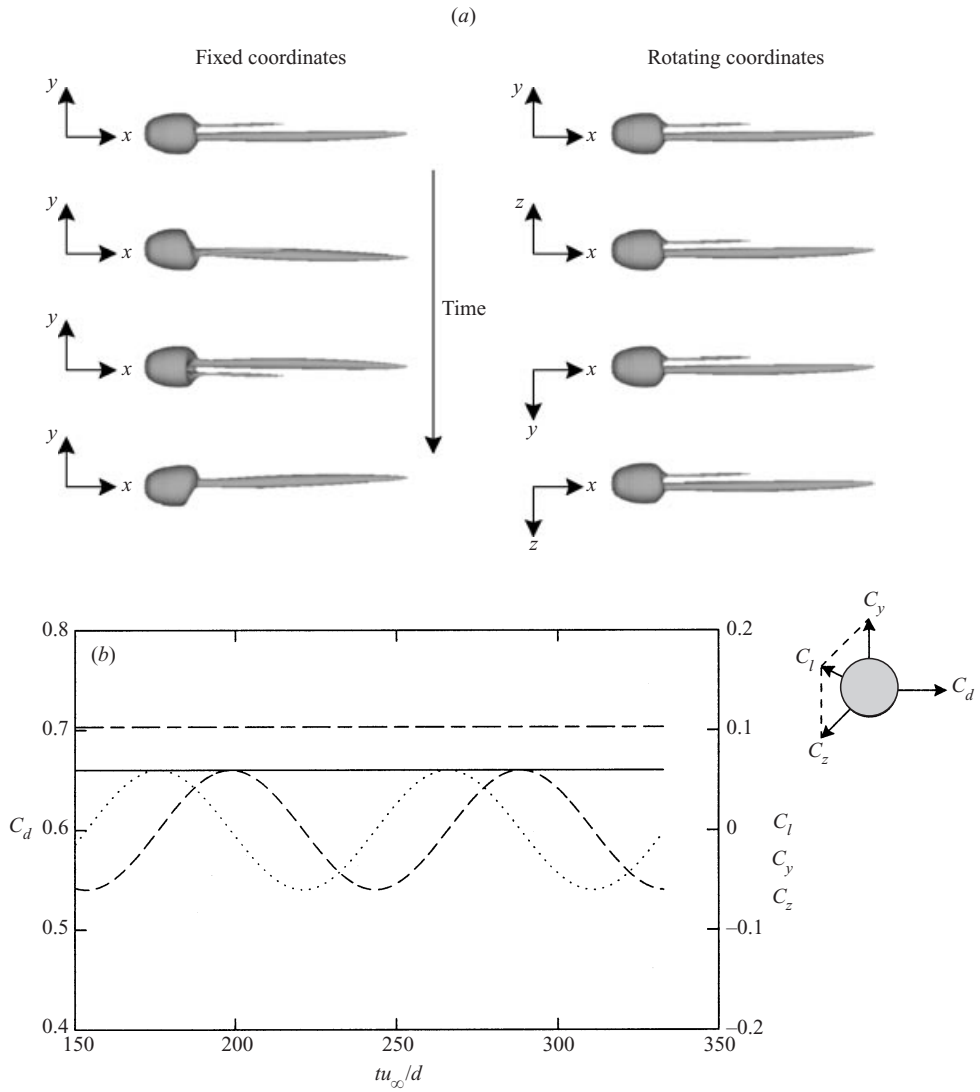


FIGURE 6. Characteristics of frozen flow at $Re = 250$ and $\omega^* = 0.1$: (*a*) temporal evolution of vortical structures viewed from a fixed coordinate system (left) and from a rotating coordinate system (right). (*b*) Drag and lift coefficients: ——, C_d; ·····, C_y; – – –, C_z; ———, C_l.

Figure 6(*a*) shows the temporal evolution of vortical structures viewed from a fixed coordinate and from a rotating coordinate at $Re = 250$ and $\omega^* = 0.1$. The rotating coordinate system rotates with a constant angular velocity the same as that of the vortical structure. The rotation velocity of the vortical structure is generally different from that of the sphere and the way of evaluating it is explained in § 4.2. It is clear from figure 6(*a*) that the vortical structure simply rotates without temporal variation in its shape and strength as if the structure were frozen (so it is called 'frozen' in this paper).† This frozen phenomenon can be verified from the time histories of the drag

† We prefer using 'frozen' to 'lock-on' (or 'phase-locked'), because the latter phenomenon usually occurs from disturbances having a certain frequency but the phenomenon described in this paper is obtained from a steady rotation.

https://doi.org/10.1017/S0022112002008509 Published online by Cambridge University Press

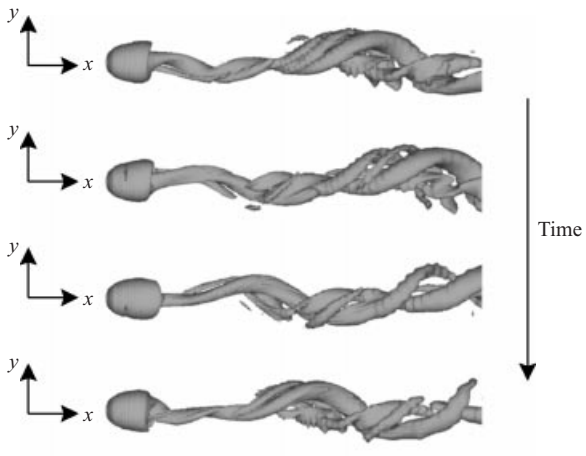


FIGURE 7. Temporal evolution of vortical structures viewed from a fixed coordinate system (unsteady asymmetric flow at $Re = 250$ and $\omega^* = 1$).

and lift coefficients shown in figure 6(b). Two components of the lift (C_y and C_z) experience sinusoidal variations, but the magnitudes of the drag and lift (C_d and C_l) are constant in time, indicating that the vortical structures in the wake simply rotate in a frozen state. Note that the time-averaged lift ($\bar{C}_y$ and $\bar{C}_z$) is zero.

When the flow is unsteady asymmetric, on the other hand, the vortical structure rotates with temporal variation in its strength. Figure 7 shows the temporal evolution of vortical structures viewed from the fixed coordinates at $Re = 250$ and $\omega^* = 1$. It is clear that the vortical structures rotate asymmetrically and convect downstream with temporal variation (so this is called 'unsteady asymmetric') unlike the frozen flow.

Figure 8 shows the modification of vortical structures due to the rotation at $Re = 300$. For a stationary sphere, the vortices are shed while the planar-symmetry of the flow is maintained. However, with the streamwise rotation, the vortical structures are significantly modified and the flow loses the planar-symmetry. For example, at $\omega^* \geqslant 0.3$, the vortices are distorted due to the rotation of the sphere and thus the head of the hairpin vortex observed for $\omega^* = 0$ completely disappears. Interestingly, at $\omega^* = 0.3$, 0.5 and 0.6, a pair of vortical structures having opposite signs of the streamwise vorticity continuously develop and spiral around the wake centreline. At $\omega^* = 1$, the vortical structures become very complicated.

The unsteady flows at $Re = 300$ can also be categorized into frozen and unsteady asymmetric flows as for $Re = 250$. At low rotational speeds ($\omega^* = 0.1$ and 0.3), the flows become unsteady asymmetric. Note that the flow at $\omega^* = 0$ is unsteady planar-symmetric. The frozen flows are obtained at $\omega^* = 0.5$ and 0.6, and the flow becomes unsteady asymmetric again at $\omega^* = 1$. It is interesting to note that the flow at $Re = 300$ becomes frozen at higher rotational speeds than that at $Re = 250$. The reason may be that the time scale of the vortices behind the stationary sphere becomes smaller at higher Reynolds number, and thus higher rotational speed is required to match the shorter time scale of the vortices in the wake.

It should be noted that there is a fundamental difference in vortical structures between the frozen flows at $Re = 250$ and 300: at $Re = 250$, the frozen flow fields ($\omega^* = 0.1$ and 0.3) contain a strong vortical structure (positive ω_x) which is elongated in the streamwise direction; however, at $Re = 300$, the vortical structures in the frozen flow fields ($\omega^* = 0.5$ and 0.6) have both positive and negative ω_x and spiral around

https://doi.org/10.1017/S0022112002008509 Published online by Cambridge University Press

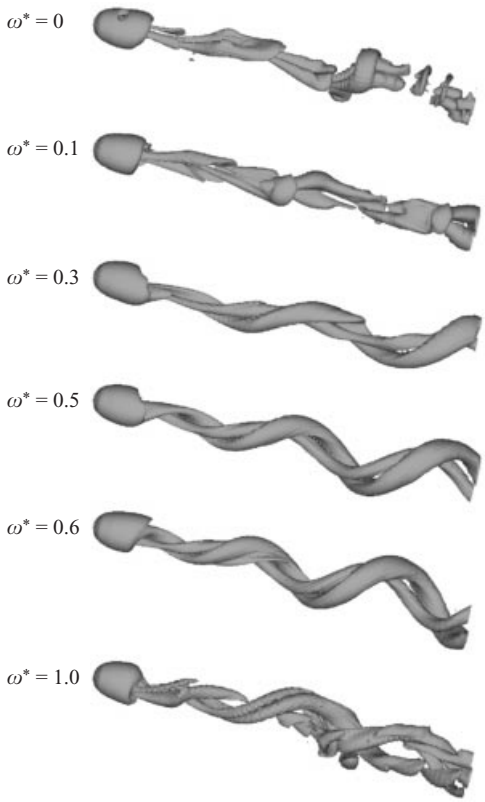


FIGURE 8. Modification of vortical structures due to the rotation at $Re = 300$.

	ω^*					
Re	0	0.1	0.3	0.5	0.6	1
100	Steady S	Steady S	Steady S	Steady S	Steady S	Steady S
250	Steady P	Frozen	Frozen	Unsteady A	Unsteady A	Unsteady A
300	Unsteady P	Unsteady A	Unsteady A	Frozen	Frozen	Unsteady A

TABLE 2. Flow regimes depending on the Reynolds number and the rotational speed. S, P and A denote, respectively, axisymmetric, planar-symmetric and asymmetric flows.

the wake centreline. Therefore, the lift characteristics of the frozen flows at $Re = 250$ and 300 are quite different from each other (see § 4.2). We expect that the frozen flow field at $Re > 300$ should be similar to that at $Re = 300$ rather than at $Re = 250$.

To summarize, the flows over a sphere with and without the streamwise rotation can be categorized into various flow regimes depending on the Reynolds number and the rotational speed as shown in table 2. The flow regimes are steady axisymmetric, steady planar-symmetric, unsteady planar-symmetric, frozen, and unsteady asymmetric. At $Re = 100$, the flow is steady axisymmetric for all the rotational speeds considered, whereas at $Re = 250$ and 300, the planar-symmetric flow changes into the asymmetric and frozen flows depending on the rotational speed.

https://doi.org/10.1017/S0022112002008509 Published online by Cambridge University Press

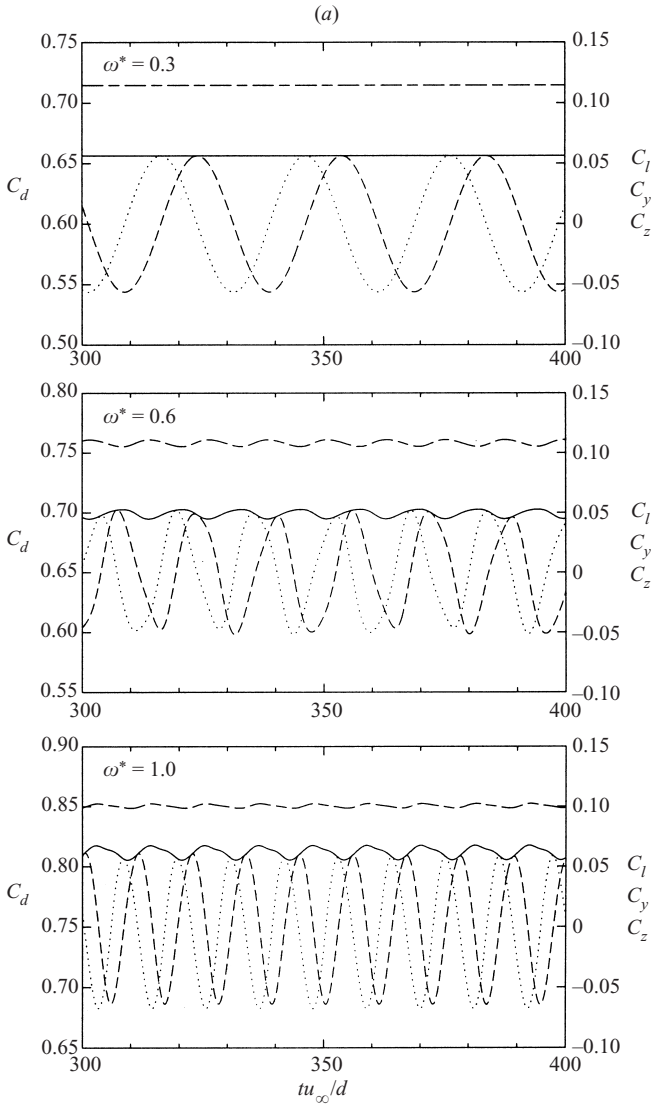


FIGURE 9(*a*). For caption see facing page.

4.2. *Drag and lift*

Figure 9 shows the time histories of the drag and lift coefficients at $Re = 250$ and 300. As mentioned before, the magnitudes of the drag and lift (C_d and C_l) are constant in time when the flow is frozen ($\omega^* = 0.1$ and 0.3 at $Re = 250$, and $\omega^* = 0.5$ and 0.6 at $Re = 300$), whereas they are time-periodic in the unsteady asymmetric flow. In the unsteady asymmetric flow, the period (T_{rep}) of C_l is the same as that of C_d, but it is not necessarily the same as that of C_y and C_z, meaning that the same pattern of vortical structures appears in the wake at every T_{rep} but at a different azimuthal angle. That is, during T_{rep}, the vortices rotate by a certain azimuthal angle while changing their strength periodically. One interesting observation is that the period of C_y and C_z in the case of the frozen flow at $Re = 300$ is shorter than that at $\omega^* = 1$, meaning that the rotational speed of the vortical structure in the frozen flow is faster

https://doi.org/10.1017/S0022112002008509 Published online by Cambridge University Press

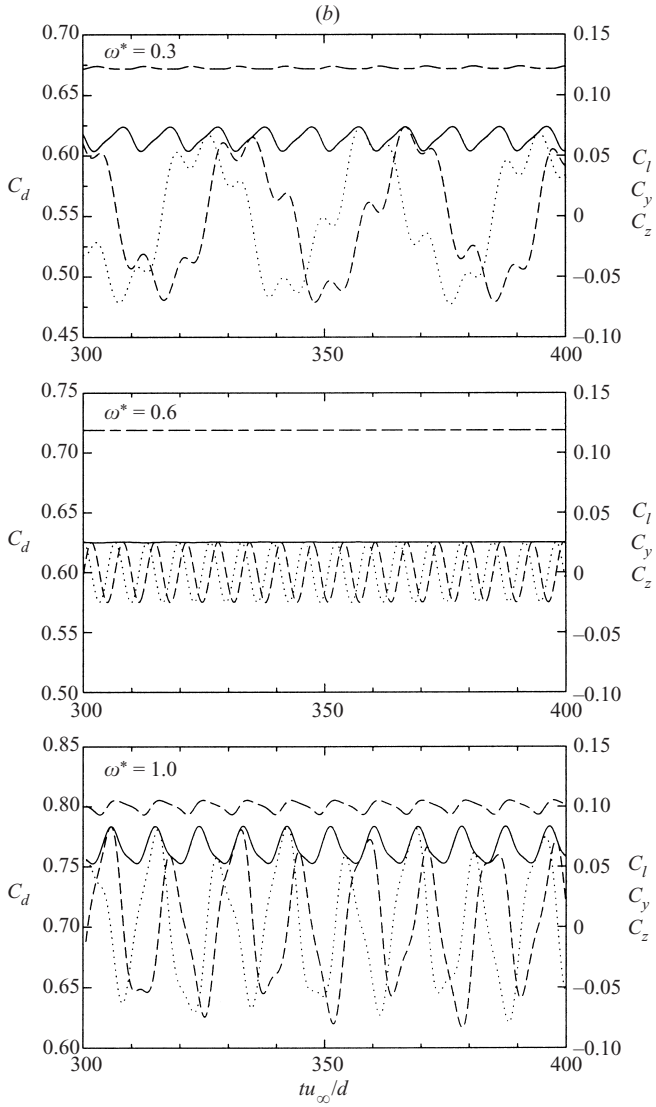


FIGURE 9. Time histories of the drag and lift coefficients: (*a*) $Re = 250$; (*b*) $Re = 300$. ———, C_d; ·····, C_y; – – – –, C_z; ———, C_l.

than that at $\omega^* = 1$, unlike the case of $Re = 250$. This difference is attributed to the different vortical structures in the frozen flows at $Re = 250$ and 300, as described before. The rotational speed of the vortices will be examined later in this section.

Figure 10 shows the effect of the rotation on the Strouhal number, $St = d/(u_\infty T_{rep})$, which is associated with the periodicity of C_d and C_l as described in figure 9. The Strouhal number is zero for frozen flow as well as steady flow because C_d and C_l are constant for both flows. At $Re = 250$, the Strouhal number is zero at $\omega^* \leqslant 0.3$, whereas it is not zero but varies little for $0.5 \leqslant \omega^* \leqslant 1$ where the flow becomes unsteady asymmetric. At $Re = 300$, on increasing the rotational speed, the Strouhal number decreases (unsteady asymmetric), becomes zero at $\omega^* = 0.5$ and 0.6 (frozen), and then increases again at $\omega^* = 1$ (unsteady asymmetric).

https://doi.org/10.1017/S0022112002008509 Published online by Cambridge University Press

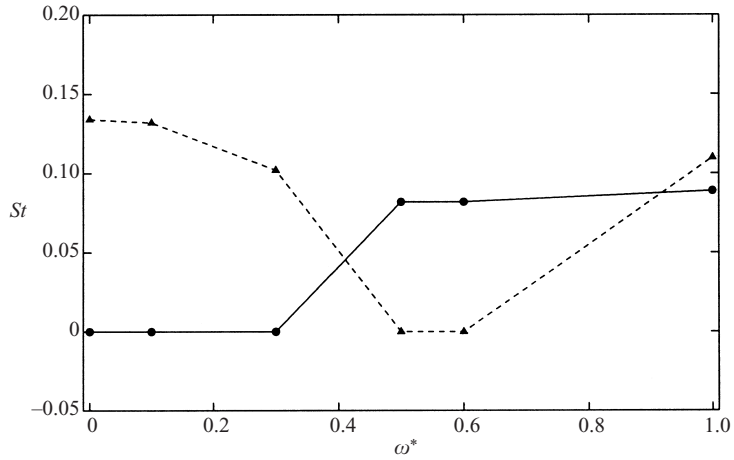


FIGURE 10. Effect of the rotation on the Strouhal number ($St = d/u_\infty T_{rep}$): ———, $Re = 250$; – – – –, $Re = 300$.

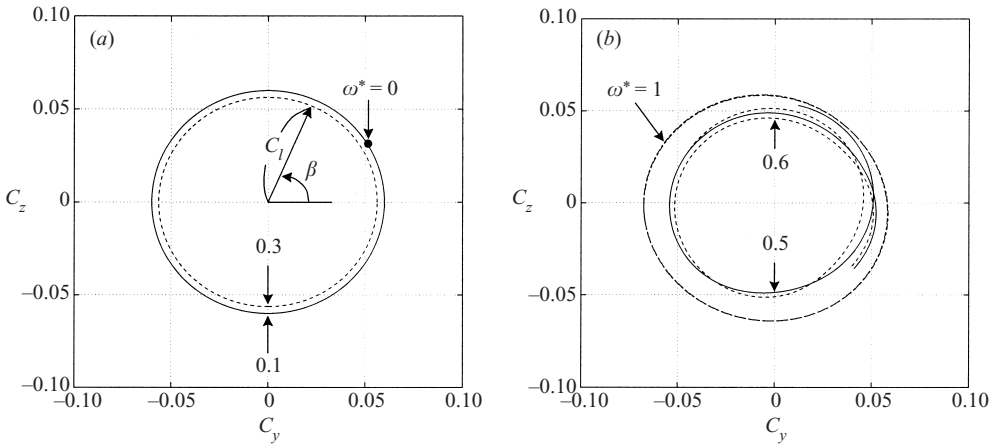


FIGURE 11. Phase diagram (C_z, C_y) at $Re = 250$: (a) steady planar-symmetric ($\omega^* = 0$) and frozen ($\omega^* = 0.1$ and 0.3) flows; (b) unsteady asymmetric flows ($\omega^* = 0.5$, 0.6 and 1).

The dynamic behaviours of the lift, both the magnitude and direction, are illustrated in the form of a phase diagram, by plotting C_z as a function of C_y as shown in figure 11. Here, for the unsteady asymmetric flow, the phase diagram is drawn for the period of $2T_{rep}$. The distance from the origin ($C_y = C_z = 0$) is equal to C_l ($= \sqrt{C_y^2 + C_z^2}$) and the angle β is the direction of the lift. At $Re = 250$, for a stationary sphere, the phase diagram falls on a point because the flow is steady (figure 11a). However, when the flow becomes frozen at $\omega^* = 0.1$ and 0.3, the phase diagram becomes a perfect circle because only the direction of the lift changes, not its magnitude, over time (figure 11a). For the unsteady asymmetric flow (figure 11b) at $\omega^* \geqslant 0.5$, the phase diagram becomes a curve turning around the origin. It is noted that at $\omega^* = 1$, the phase diagram becomes a closed curve but not a circle.

Figure 12 shows the phase diagram (C_z, C_y) at $Re = 300$, drawn for the period $13T_{rep}$ for the unsteady asymmetric flow. Without the streamwise rotation ($\omega^* = 0$), the flow is unsteady planar-symmetric and thus the magnitude of the lift oscillates

https://doi.org/10.1017/S0022112002008509 Published online by Cambridge University Press

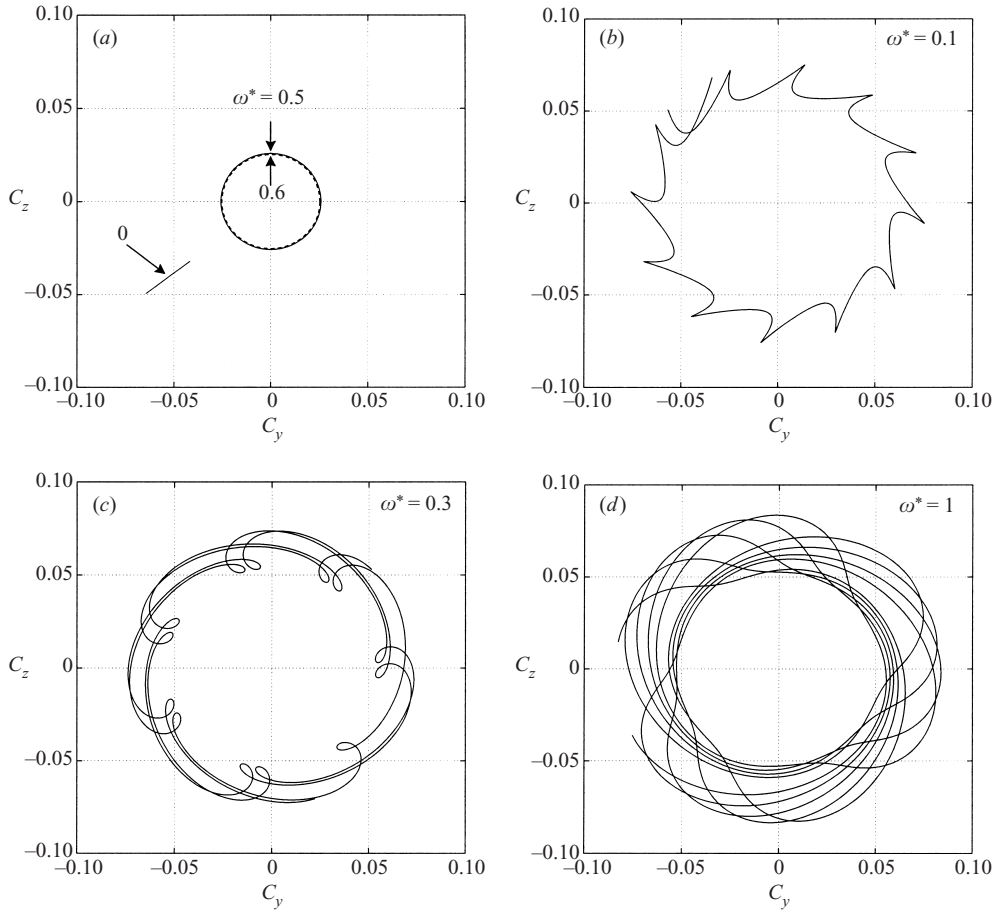


FIGURE 12. Phase diagram (C_z, C_y) at $Re = 300$: (a) unsteady planar-symmetric ($\omega^* = 0$) and frozen ($\omega^* = 0.5$ and 0.6) flows; (b) $\omega^* = 0.1$; (c) $\omega^* = 0.3$; (d) $\omega^* = 1$. (b), (c) and (d) correspond to unsteady asymmetric flows.

on a straight line on the phase diagram. At $\omega^* = 0.5$ and 0.6, the phase diagrams become perfect circles because the flows are frozen. The radii of the circles at $\omega^* = 0.5$ and 0.6 are nearly the same, as shown in figure 12(a). On the other hand, when the flow becomes unsteady asymmetric at $\omega^* = 0.1$, 0.3 and 1, both the magnitude and direction of the lift change over time and the phase diagram turns around the origin.

As shown in the previous section, the vortical structures past a sphere rotate in the same direction as the rotation of the sphere. However, the rotation speed of the vortical structures is quite different from that of the sphere. The time history of the lift angle β is used to evaluate the rotation speed of the vortical structures, because it is closely associated with the rotation of the vortical structures. Figures 13(a) and 13(b) show the time histories of the lift angle β, respectively for the frozen and unsteady asymmetric flows, where the slope of β with respect to t corresponds to the rotation velocity of the vortical structures. As seen in figure 13(a), the vortical structures rotate at a constant speed when the flow is frozen. However, when the flow is unsteady asymmetric, they do not have a constant rotation speed (figure 13b). Therefore, in this case, the rotation velocity of the vortical structures is estimated in a time-averaged sense.

https://doi.org/10.1017/S0022112002008509 Published online by Cambridge University Press

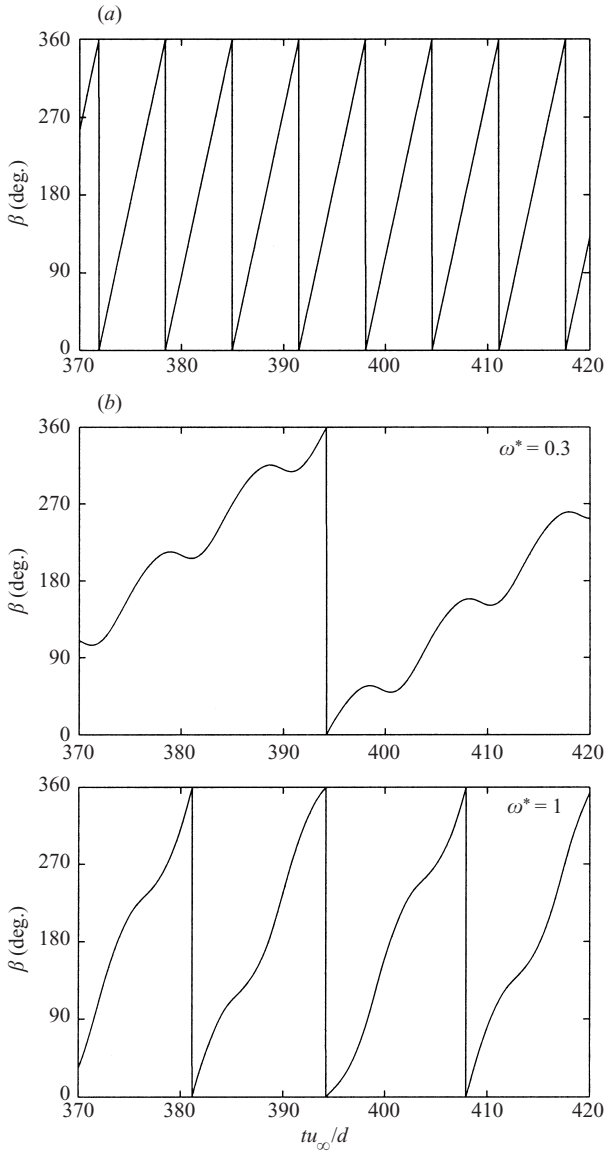


FIGURE 13. Time histories of the lift angle β at $Re = 300$: (a) frozen flow ($\omega^* = 0.6$); (b) unsteady asymmetric flow ($\omega^* = 0.3$ and 1).

The period of β is denoted as T_{rev} and it is equivalent to the time for the vortical structures to complete one revolution. Note that T_{rev} is not equal to T_{rep}. Figure 14(a) shows the revolution time T_{rev} as a function of the rotational speed. When normalized by d/u_∞, the revolution time at $Re = 250$ decreases with increasing rotational speed, indicating that the vortical structures rotate faster at higher ω^*. However, at $Re = 300$, the revolution times for the frozen flows ($\omega^* = 0.5$ and 0.6) are smaller than that at $\omega^* = 1$, meaning that the vortical structures in the frozen flow at $Re = 300$ rotate faster than those at $\omega^* = 1$. The difference in the variations of T_{rev} with respect to ω^* at $Re = 250$ and 300 is again attributed to the significant difference in the vortical structures at $Re = 250$ and 300. Figure 14(b) shows the ratio of the revolution time

https://doi.org/10.1017/S0022112002008509 Published online by Cambridge University Press

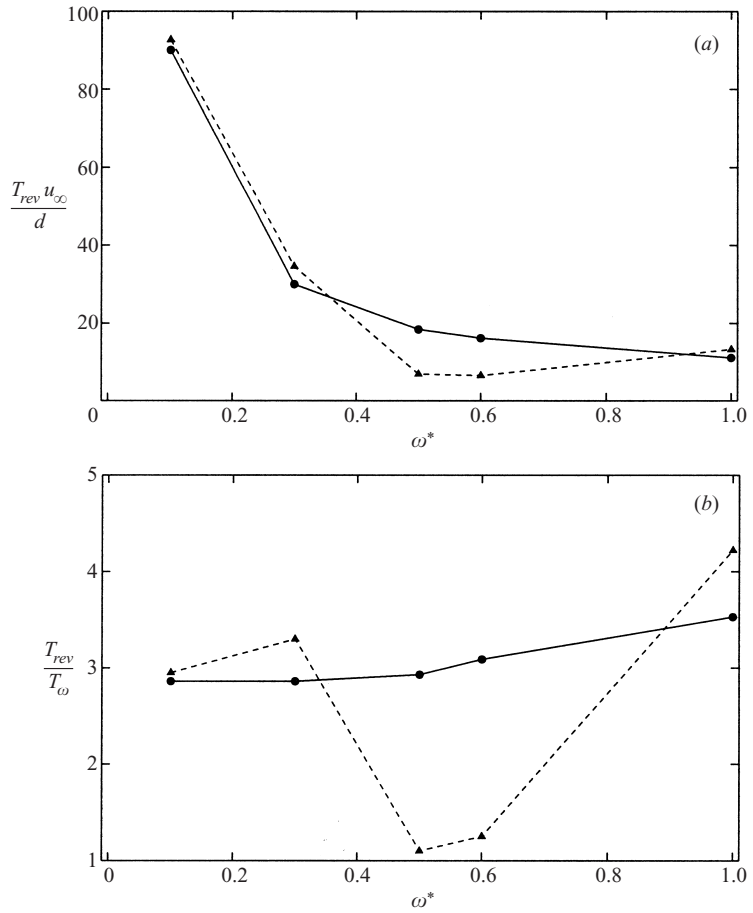


FIGURE 14. Time for the vortical structure to complete one revolution: (*a*) normalized by d/u_∞; (*b*) normalized by the time for the sphere to rotate by 360°. ———, $Re = 250$; – – – –, $Re = 300$.

of the vortical structures to that of the sphere (T_ω). It is seen that $T_{rev}/T_\omega > 1$ for all the rotational speeds considered, indicating that the revolution speed of the vortices is slower than that of the sphere. The ratio T_{rev}/T_ω increases monotonically with increasing rotational speed at $Re = 250$, whereas at $Re = 300$ it shows a local minimum when the flow is frozen. It is also interesting to note that the ratio becomes nearly 1 when the flow is frozen, meaning that the vortical structures rotate nearly in phase with the rotating sphere as if they had almost attained a solid-body rotation.

The dynamic behaviours of the drag and lift forces are investigated from the phase diagram (C_l, C_d) as shown in figure 15. Note that C_l is the magnitude of the lift coefficient without considering its direction ($C_l = \sqrt{C_y^2 + C_z^2}$) and thus the time-averaged C_l is not necessarily zero even if the time-averaged C_y or C_z is zero. The phase diagram takes the form of a closed curve for the unsteady planar-symmetric and unsteady asymmetric flows, whereas it falls on a point for the steady and frozen flows (in the frozen flow, C_d and C_l are constant even though the direction of the lift changes in time). The closed curves for the unsteady flows suggest that the flows are time-periodic. Also, the position of the curve indicates the time-averaged values of C_d and C_l, and its size denotes the fluctuation amplitudes. Therefore, it is clear

https://doi.org/10.1017/S0022112002008509 Published online by Cambridge University Press

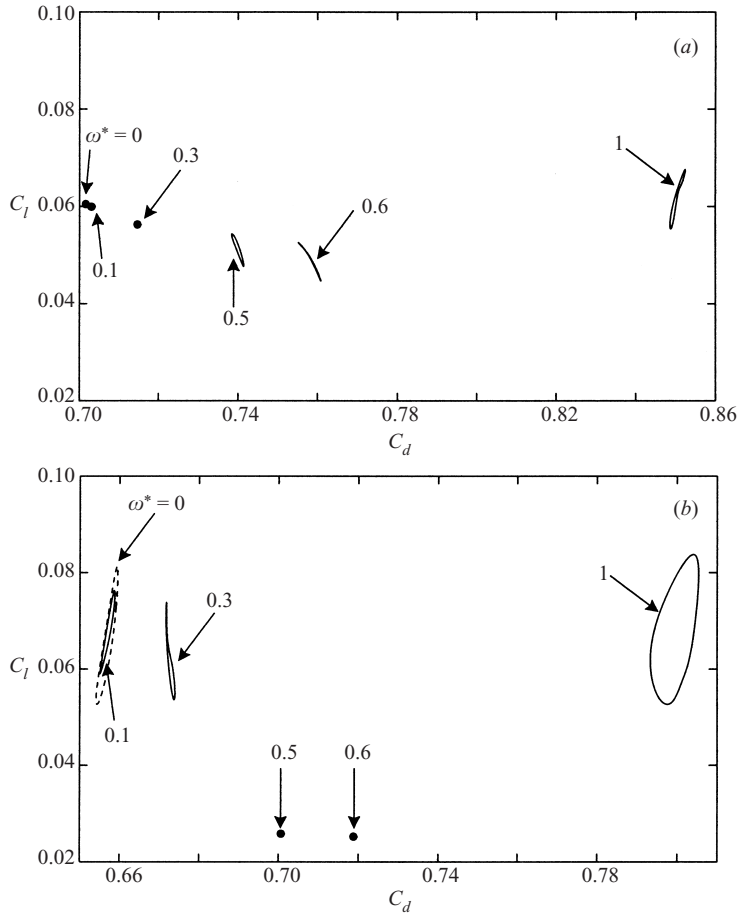


FIGURE 15. Phase diagram (C_l, C_d): (*a*) $Re = 250$; (*b*) $Re = 300$ ($\omega^* = 0$ is drawn with a dashed line for clear comparison).

from figure 15 that $\bar{C}_d$ increases with increasing rotational speed for both Reynolds numbers, whereas $\bar{C}_l$ shows a non-monotonic behaviour with respect to the rotational speed (see below). The fluctuation amplitude of C_l is larger than that of C_d and increases with increasing rotational speed for the unsteady asymmetric flow. When the flow is frozen, the fluctuations of C_d and C_l are zero.

Figure 16 shows the variations of the time-averaged C_d and C_l with respect to the rotational speed. For a given Reynolds number, $\bar{C}_d$ increases with increasing rotational speed, whereas it decreases with increasing Reynolds number for a given rotational speed. On the other hand, $\bar{C}_l$ shows a non-monotonic behaviour as shown in figure 16(*b*). At $Re = 100$, $\bar{C}_l$ is zero for all the rotational speeds investigated because the flow maintains axisymmetry. However, at $Re = 250$ and 300, $\bar{C}_l$ first decreases and then increases with increasing rotational speed. It is interesting to note that $\bar{C}_l$ is very low at $Re = 300$ when the flow is frozen, which is not true at $Re = 250$. The reason is that at $Re = 250$, the frozen flow contains a strong and elongated vortical structure whose centre is not aligned with the wake centreline, and thus $\bar{C}_l$ for the frozen flow is not smaller than those at $\omega^* = 0.5$ and 0.6, at which the strong vortical structure twists around the wake centreline (see figure 5).

https://doi.org/10.1017/S0022112002008509 Published online by Cambridge University Press

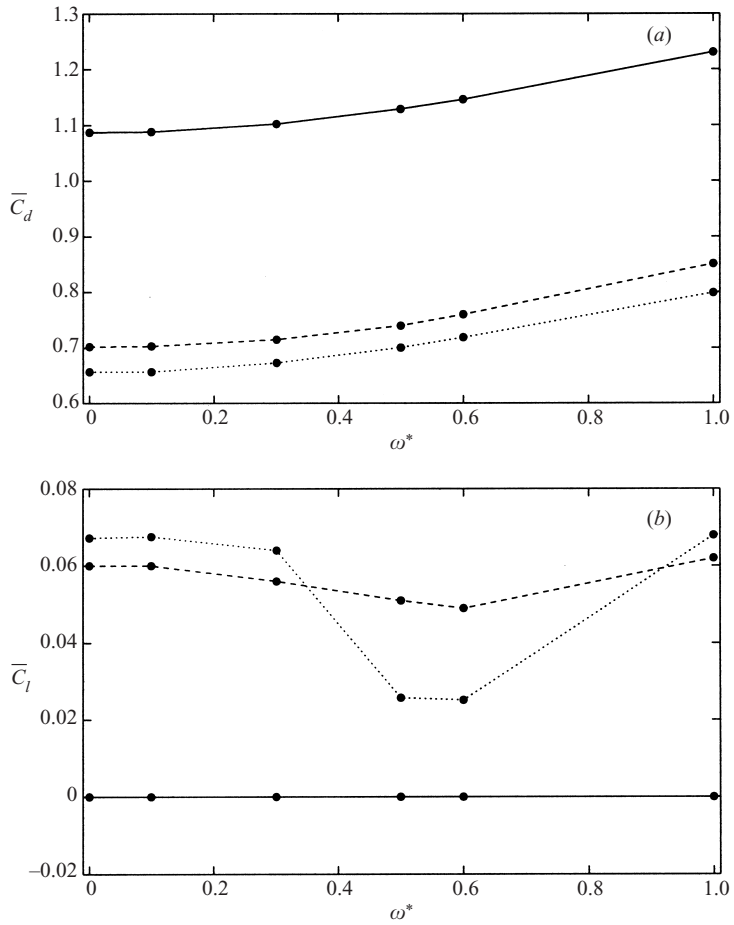


FIGURE 16. Variations of the time-averaged C_d and C_l with respect to the rotational speed: (*a*) $\bar{C}_d$; (*b*) $\bar{C}_l$. ———, $Re = 100$; – – – –, $Re = 250$; · · · · · ·, $Re = 300$.

Figure 17 shows the variation of the pressure coefficient ($C_p = (p - p_\infty)/\frac{1}{2}\rho u_\infty^2$) along the sphere surface with respect to the rotational speed at $Re = 300$, where p_∞ is the pressure in the free stream and C_p is an averaged value in time and azimuthal direction. The pressure at the rear of the sphere decreases with increasing rotational speed, whereas it is nearly unchanged at the front of the sphere. Therefore, the pressure drag increases with increasing rotational speed. Similar observations are made for $Re = 100$ and 250.

Figure 18 shows the variations of the separation angle (α_s) and the size of the recirculation region (L) with respect to the rotational speed, where α_s is the separation angle from the front stagnation point of the sphere. Without the streamwise rotation ($\omega^* = 0$), the separation line moves upstream on the sphere surface with increasing Reynolds number. The separation line also moves upstream with increasing rotational speed for all the Reynolds numbers considered, which is in good agreement with the result of Hoskin (1955). However, the effect of the rotation on the size of the recirculation region depends on the Reynolds number, where the size of the recirculation region is estimated as the distance from the base of the sphere to the point where the time-averaged streamwise velocity is zero. The size of the recirculation

https://doi.org/10.1017/S0022112002008509 Published online by Cambridge University Press

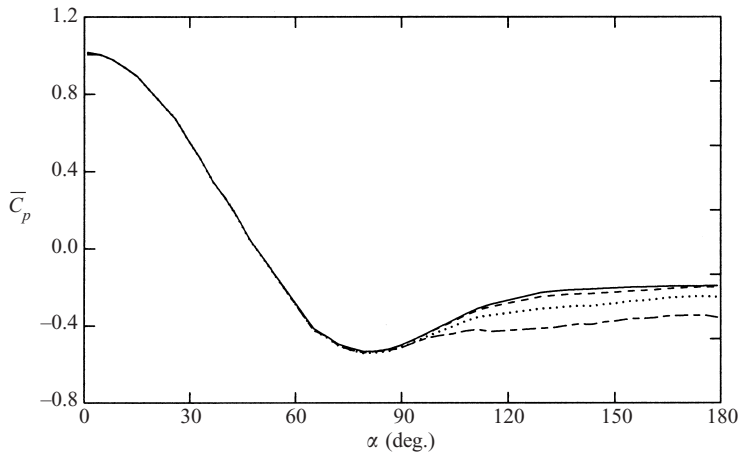


FIGURE 17. Variation of the pressure coefficient along the sphere surface with respect to the rotational speed at $Re = 300$: ———, $\omega^* = 0$; – – – –, $\omega^* = 0.3$; · · · · · ·, $\omega^* = 0.6$; — – —, $\omega^* = 1$.

region increases with increasing rotational speed at $Re = 100$ and 250, whereas at $Re = 300$ the size of the recirculation region shows a local minimum when the flow is frozen. This different behaviour is again associated with the difference in vortex formation in the wake at those Reynolds numbers.

5. Summary and concluding remarks

Laminar flow past a sphere rotating in the streamwise direction was simulated using an immersed boundary method in order to investigate the effect of the streamwise rotation on the vortical structures behind the sphere as well as the drag and lift forces exerted on the sphere. Numerical simulations were performed at $Re = 100$, 250 and 300 in the range of $0 \leqslant \omega^* \leqslant 1$. The results showed that the flow around the sphere strongly depends on both the Reynolds number and the rotational speed.

The flows over a sphere with and without the streamwise rotation were categorized into various flow regimes: steady axisymmetric, steady planar-symmetric, unsteady planar-symmetric, frozen and unsteady asymmetric. At $\omega^* = 0$ (without rotation), the flow past the sphere was steady axisymmetric, steady planar-symmetric, and unsteady planar-symmetric, respectively, at $Re = 100$, 250 and 300. With the streamwise rotation, the flow changed into steady axisymmetric, frozen, and unsteady asymmetric flows depending on the Reynolds number and the rotational speed.

The three-dimensional vortical structures behind the sphere were significantly modified by the streamwise rotation. For example, the vortical structures at $Re = 300$ were completely changed due to the rotation and the flow became frozen at $\omega^* = 0.5$ and 0.6. When the flow became frozen, the vortical structures behind the sphere simply rotated without temporal variation of their strength, and the magnitudes of the drag and lift were constant in time. As the Reynolds number increased, the flow became frozen at larger rotational speed. On the other hand, when the flow was unsteady asymmetric, the vortical structures rotated with temporal variation of their strength. The rotation speed of the vortical structures was also estimated, showing that it is slower than that of the sphere for all the rotational speeds considered.

When the rotational speed increased, the time-averaged drag coefficient increased, whereas the time-averaged lift coefficients ($\bar{C}_y$ and $\bar{C}_z$) were zero for all $\omega^* > 0$. Meanwhile, the time-averaged magnitude of the lift coefficients ($\bar{C}_l$) showed a non-

https://doi.org/10.1017/S0022112002008509 Published online by Cambridge University Press

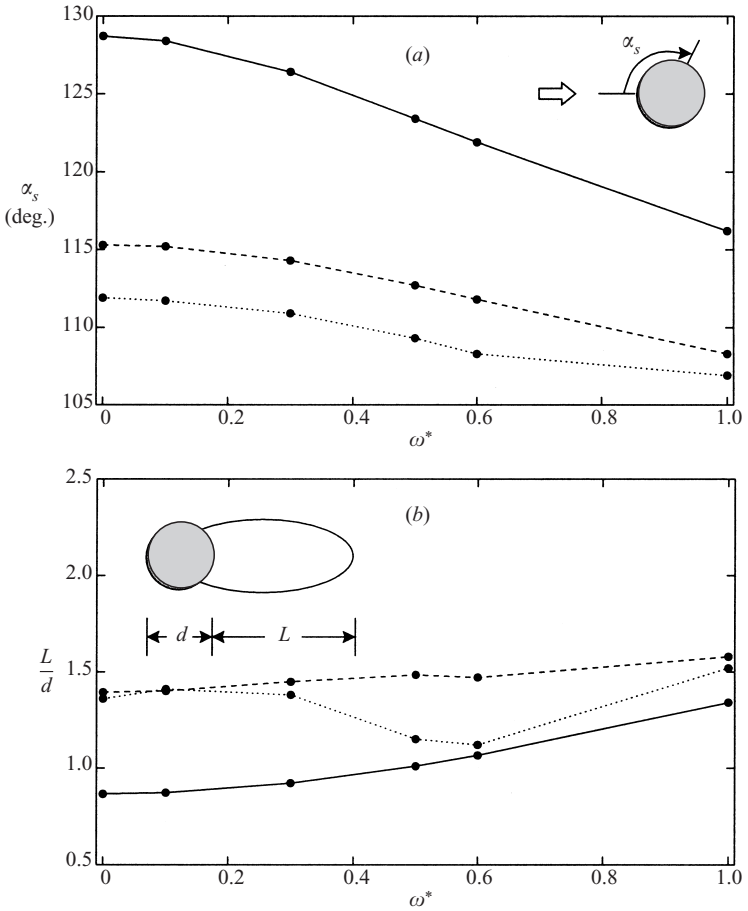


FIGURE 18. Variations of the separation angle (α_s) and the size of the recirculation region (L) with respect to the rotational speed: (*a*) α_s; (*b*) L. ———, $Re = 100$; – – – –, $Re = 250$; · · · · · ·, $Re = 300$.

monotonic behaviour depending on the Reynolds number. At $Re = 100$, the flow past the sphere showed steady axisymmetry for all the rotational speeds and thus $\bar{C}_l$ was zero. On the other hand, at $Re = 250$ and 300, the flows were unsteady with rotation. With increasing rotational speed, $\bar{C}_l$ first decreased and then increased, showing a local minimum at a specific rotational speed.

From the present study, we have observed a phenomenon termed 'frozen' in the wake behind a rotating sphere at $Re \leqslant 300$. In this Reynolds number range, the flow behind a stationary sphere is either steady or unsteady planar-symmetric. At a higher Reynolds number, however, the flow behind a stationary sphere becomes unsteady asymmetric and thus a different type of 'frozen' flow may be observed with a rotating sphere, which should be an important subject for future study.

This work is supported by the Creative Research Initiatives of the Korean Ministry of Science and Technology.

REFERENCES

AKSELVOLL, K. & MOIN, P. 1996 An efficient method for temporal integration of the Navier–Stokes equations in confined axisymmetric geometries. *J. Comput. Phys.* **125**, 454–463.

https://doi.org/10.1017/S0022112002008509 Published online by Cambridge University Press

Barkla, H. M. & Auchterlonie, L. J. 1971 The Magnus and Robins effect on rotating spheres. *J. Fluid Mech.* **47**, 437–447.

Choi, M.-R. 1998 Characteristics of a transitional boundary layer on a flat plate using a direct numerical simulation technique. PhD dissertation, Seoul National University.

Constantinescu, G. S. & Squires, K. D. 2000 LES and DES investigations of turbulent flow over a sphere. *AIAA Paper* 2000-0540.

Fadlun, E. A., Verzicco, R., Orlandi, P. & Mohd-Yusof, J. 2000 Combined immersed-boundary finite-difference methods for three-dimensional complex flow simulations. *J. Comput. Phys.* **161**, 35–60.

Fornberg, B. 1988 Steady viscous flow past a sphere at high Reynolds numbers. *J. Fluid Mech.* **190**, 471–489.

Hoskin, N. E. 1955 The laminar boundary layer on a rotating sphere. In *Fifty Years of Boundary Layer Research*, pp. 127–131. Braunschweig.

Jeong, J. & Hussain, F. 1995 On the identification of a vortex. *J. Fluid Mech.* **285**, 69–94.

Johnson, T. A. & Patel, V. C. 1999 Flow past a sphere up to a Reynolds number of 300. *J. Fluid Mech.* **378**, 19–70.

Kim, J., Kim, D. & Choi, H. 2001 An immersed-boundary finite volume method for simulations of flow in complex geometries. *J. Comput. Phys.* **171**, 132–150.

Kurose, R. & Komori, S. 1999 Drag and lift forces on a rotating sphere in a linear shear flow. *J. Fluid Mech.* **384**, 183–206.

Luthander, S. & Rydberg, A. 1935 Experimentelle untersuchungen uber den luftwiderstand bei einer um eine mit der windrichtung parallele achse rotierenden kugel. *Phys. Z.* **36**, 552–558.

Mittal, R. 1999*a* A Fourier–Chebyshev spectral collocation method for simulating flow past spheres and spheroids. *Intl J. Numer. Meth. Fluids* **30**, 921–937.

Mittal, R. 1999*b* Planar symmetry in the unsteady wake of a sphere. *AIAA J.* **37**, 388–390.

Oesterlé, B. & Dinh, T. B. 1999 Experiments on the lift of a spinning sphere in a range of intermediate Reynolds numbers. *Exps. Fluids* **25**, 16–22.

Rubinow, S. I. & Keller, J. B. 1961 The transverse force on a spinning sphere moving in a viscous fluid. *J. Fluid Mech.* **11**, 447–459.

Sakamoto, H. & Haniu, H. 1990 A study on vortex shedding from spheres in a uniform flow. *Trans. ASME*: *J. Fluids Engng* **112**, 386–392.

Schlichting, H. 1979 *Boundary Layer Theory*, 7th Edn. McGraw-Hill.

Shirayama, S. 1992 Flow past a sphere: topological transitions of the vorticity field. *AIAA J.* **30**, 349–358.

Tomboulides, A. & Orszag, S. 2000 Numerical investigation of transitional and weak turbulent flow past a sphere. *J. Fluid Mech.* **416**, 45–73.

Tsuji, Y., Morikawa, Y. & Mizuno, O. 1985 Experimental measurement of the Magnus force on a rotating sphere at low Reynolds numbers. *Trans. ASME: J. Fluids Engng* **107**, 484–488.

Zhou, J., Adrian, R. J., Balachandar, S. & Kendall, T. M. 1999 Mechanisms for generating coherent packets of hairpin vortices in channel flow. *J. Fluid Mech.* **387**, 353–396.

https://doi.org/10.1017/S0022112002008509 Published online by Cambridge University Press